Stoichiometry and compositional plasticity of the yeast nuclear pore complex revealed by quantitative fluorescence microscopy

Sasikumar Rajoo[a,b,1], Pascal Vallotton[a,1], Evgeny Onischenko[a], and Karsten Weis[a,2]

[a]Institute of Biochemistry, Department of Biology, Swiss Federal Institute of Technology Zurich, CH-8093 Zurich, Switzerland; and [b]Molecular Life Science PhD Program, Life Science Zurich Graduate School, CH-8057 Zurich, Switzerland

Edited by Jodi Nunnari, University of California, Davis, CA, and approved March 16, 2018 (received for review November 8, 2017)

The nuclear pore complex (NPC) is an eightfold symmetrical channel providing selective transport of biomolecules across the nuclear envelope. Each NPC consists of ∼30 different nuclear pore proteins (Nups) all present in multiple copies per NPC. Significant progress has recently been made in the characterization of the vertebrate NPC structure. However, because of the estimated size differences between the vertebrate and yeast NPC, it has been unclear whether the NPC architecture is conserved between species. Here, we have developed a quantitative image analysis pipeline, termed nuclear rim intensity measurement (NuRIM), to precisely determine copy numbers for almost all Nups within native NPCs of budding yeast cells. Our analysis demonstrates that the majority of yeast Nups are present at most in 16 copies per NPC. This reveals a dramatic difference to the stoichiometry determined for the human NPC, suggesting that despite a high degree of individual Nup conservation, the yeast and human NPC architecture is significantly different. Furthermore, using NuRIM, we examined the effects of mutations on NPC stoichiometry. We demonstrate for two paralog pairs of key scaffold Nups, Nup170/Nup157 and Nup192/Nup188, that their altered expression leads to significant changes in the NPC stoichiometry inducing either voids in the NPC structure or substitution of one paralog by the other. Thus, our results not only provide accurate stoichiometry information for the intact yeast NPC but also reveal an intriguing compositional plasticity of the NPC architecture, which may explain how differences in NPC composition could arise in the course of evolution.

nuclear pore complex | nucleoporins | stoichiometry | quantitative fluorescence microscopy | NPC composition

In eukaryotes, chromosomes reside in the nucleus, a dedicated cellular compartment that is delimited by the inner and outer membrane of the nuclear envelope (NE). The transport across this membrane barrier is made possible by nuclear pore complexes (NPCs)—huge channels that span and merge the inner and outer nuclear membranes (1). Despite an estimated mass of 60–120 MDa, NPCs are assembled from only ∼30 different building blocks called nucleoporins (Nups) (2–5). NPCs display an axial eightfold symmetry (6) such that individual Nups are expected to be present in multiples of eight copies (i.e., 8, 16, 24, etc.), and each NPC is therefore composed of 500–1,000 proteins, ultimately accounting for its large mass (7–10).

Significant progress has been made in the last few years in the structural characterization of components of the NPC. X-ray crystallography has provided an inventory of atomic structures for a large number of individual Nups, and also for many Nup complexes that form stable subassemblies (11, 12). For example, the Y complex (or Nup84 complex), comprising a single copy of each Nup84, Seh1, Nup85, Nup120, Sec13, Nup145C, and Nup133, has been extensively characterized both biochemically and structurally (13–15). It is expected that members of subcomplexes such as the Y complex have the same stoichiometry within the context of intact NPCs as they have in vitro, and thus for the Y complex an abundance ratio of 1:1:1:1:1:1:1 is predicted. Furthermore, several groups have analyzed the overall stoichiometry of Nups within the NPC (4, 7, 8, 16–19). Notably, a combination of mass spectrometry and fluorescent quantification was used to conclude that the human NPC consists of 32 copies of most scaffold Nups, including all members of the Y complex (18). Additionally, remarkable advances in cryo-electron tomography have allowed for detailed structural characterization of intact NPCs exemplified by current structures for *Xenopus* and human NPCs at resolutions of ∼20 and ∼23 Å, respectively (20, 21). The EM maps together with stoichiometry data, structural information, genetic data from yeast, and a large body of biochemical interaction studies were recently integrated to produce the first molecular models for the whole human NPC scaffold architecture (22, 23).

Whereas individual Nups and Nup subcomplexes are generally well conserved throughout evolution, it is unclear whether the structural model of the human NPC can be applied to all eukaryotes. For example, the molecular mass of the budding yeast NPC was measured in the 60-MDa range compared with 100–130 MDa for the vertebrate NPC (24–27). Additionally, cryo-electron reconstructions show that the yeast NPC is smaller and flatter in comparison with its vertebrate counterpart (25). Careful examination of Nup stoichiometries will be critical to understanding the basis of such evolutionary differences.

Significance

The nuclear pore complex (NPC) is one of the largest protein assemblies in eukaryotes comprising over 500 nucleoporin subunits. The NPC is essential for the transport of biomolecules across the nuclear envelope; however, due to its enormous size, it has been a challenge to characterize its molecular architecture. Herein, we have developed a widely applicable imaging pipeline to determine the absolute nucleoporin abundances in native yeast NPCs. This reveals that the NPC composition dramatically differs between yeast and humans despite overall conservation of individual subunits. We also applied our imaging pipeline to examine yeast mutants revealing remarkable compositional plasticity of NPCs. Our stoichiometry analyses provide an important resource for the generation of high-resolution structure models of the NPC.

Author contributions: S.R., P.V., E.O., and K.W. designed research; S.R., P.V., and E.O. performed research; S.R. and P.V. contributed new reagents/analytic tools; S.R. and P.V. analyzed data; and S.R., P.V., E.O., and K.W. wrote the paper.

The authors declare no conflict of interest.

This article is a PNAS Direct Submission.

Published under the PNAS license.

[1]S.R. and P.V. contributed equally to this work.

[2]To whom correspondence should be addressed. Email: karsten.weis@bc.biol.ethz.ch.

This article contains supporting information online at www.pnas.org/lookup/suppl/doi:10.1073/pnas.1719398115/-/DCSupplemental.

Published online April 9, 2018.

CELL BIOLOGY

Downloaded by guest on February 24, 2022

Moreover, reliable copy number information for every Nup is essential to produce faithful 3D models of the NPC structure as stoichiometry together with symmetry information underlies the entire process of fitting the electron density of individual subunits into experimental EM maps (28).

In this study, we have used a library of yeast strains expressing endogenously GFP-tagged Nups to accurately determine Nup copy numbers within the intact NPC. To this end, we have developed a high-throughput automated fluorescence imaging technique, which we termed nuclear rim intensity measurement (NuRIM). This allowed us to obtain relative Nup stoichiometries based on the precise quantification of fluorescence intensities at the NE. Comparison of the intensity of selected Nups at the single NPC level with well-characterized fluorescence intensity standards allowed us to obtain the absolute copy numbers for almost all Nups in yeast. Remarkably, our results show that most of the Nups in yeast are present in only half the copy number compared with their mammalian counterparts (22, 23), thus

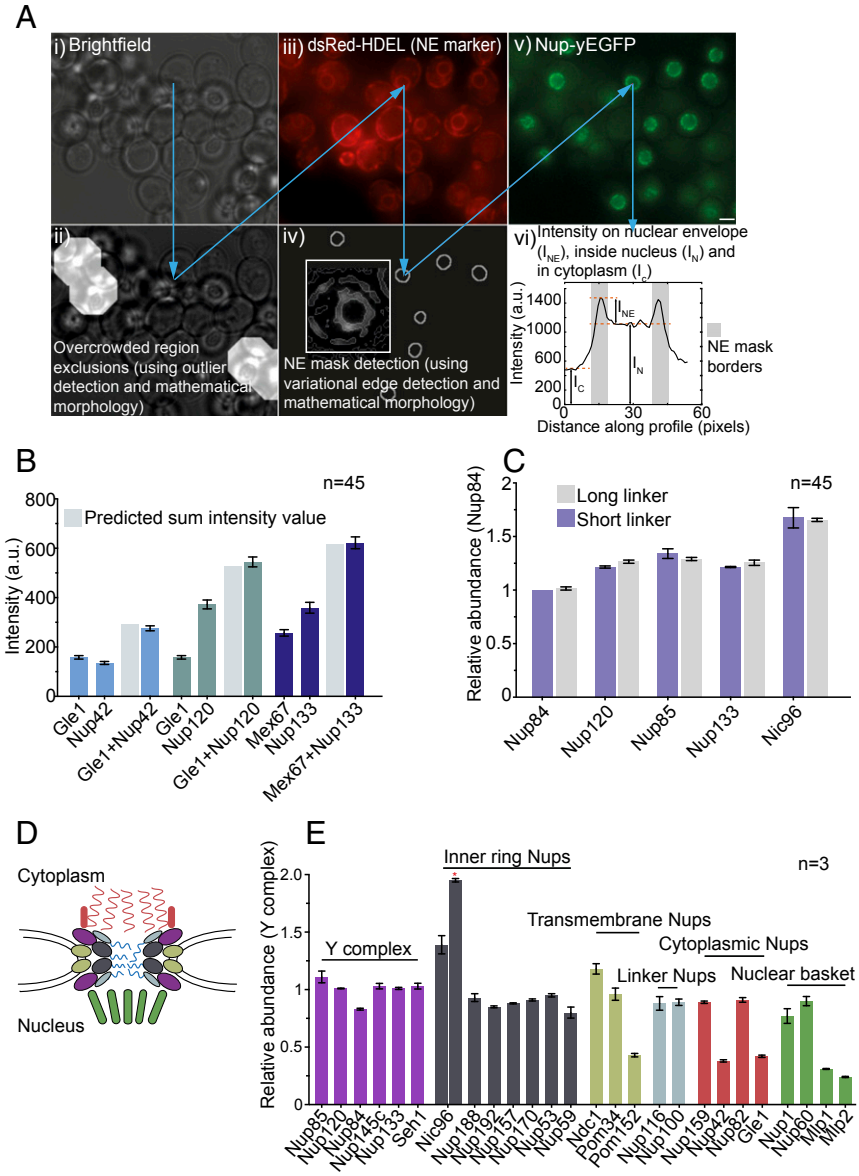

Fig. 1. Analysis of the relative NPC stoichiometry. (*A*) Outline of the nuclear rim intensity measurement (NuRIM) technique. (*A*, *i*–*vi*) Cells coexpressing dsRed-HDEL and various GFP-tagged Nups were imaged sequentially in bright-field, dsRed, and GFP channels. (*A*, *i*) Bright-field channel shows localization of immobilized yeast cells. (*A*, *ii*) Exclusion of the overcrowded regions (light areas) based on the bright-field images. (*A*, *iii*) dsRed-HDEL channel shows localization of dsRed-HDEL marking the NEs. (*A*, *iv*) Production of binary NE contour masks based on the dsRed images. (*A*, *v*) GFP channel showing localization of endogenously GFP-tagged Nups. (*A*, *vi*) Background-subtracted Nup-GFP intensities are measured and averaged across thousands of binary NE contours. (Scale bars: 2 μm.) (*B*) Linearity of GFP-based intensity measurements. Cells expressing indicated yEGFP-tagged Nups alone or in pairwise combinations were imaged in parallel. Corresponding NE signal intensities were quantified using NuRIM. Gray bars represent corresponding arithmetic sums of the NE signal intensities of singly labeled strains. Mean ± SD. *n*, number of image frames analyzed. (*C*) Robustness of GFP-based intensity measurements against microenvironmental variability. Intensity values obtained using NuRIM for the indicated Nups with C-terminal yEGFP tag separated by 6- or 102-aa linker sequence. Intensity values were normalized to Nup84-yEGFP containing a short linker. Mean ± SD. *n*, number of image frames analyzed. (*D*) Schematic representation of the NPC. Nup subgroups are depicted as colored cartoons. (*E*) Relative abundance of yeast Nups. NE intensities for the indicated yEGFP-tagged Nups were quantified using NuRIM and normalized for the average value obtained for the six components of the Y complex. *Relative abundance for GFP-Nic96 was obtained from independent measurements normalized to Nup120-GFP. Mean ± SD. *n*, number of independent experiments performed on different days.

Downloaded by guest on February 24, 2022

identifying a striking difference in the composition of yeast and vertebrate NPCs. Furthermore, by exploiting our workflow, we found that altering Nup expression levels led to the formation of functional NPCs with significantly altered stoichiometries revealing an astonishing plasticity of NPC architecture.

Results

NuRIM: A Quantitative Live-Cell Imaging Assay to Determine the Relative Stoichiometry of GFP-Tagged Nups Within Intact NPCs. Relative abundances (i.e., stoichiometries) of Nups were comprehensively evaluated both in vertebrate cells and in budding yeast using bulk biochemical methods such as mass spectrometry (18) or quantitative SDS/PAGE (4). These methods rely on biochemical purifications where it is difficult to ensure and assess the integrity of the NPC preparations. By contrast, fluorescence-imaging approaches have the potential to determine Nup abundances within intact NPCs in living cells. If the tags do not interfere with NPC incorporation, comparisons of average intensities over many NPCs within many NEs expressing different GFP-tagged Nups should provide very accurate relative abundance information. For example, a Nup present at twice the copy number of another should yield an average intensity value at the NE differing by a factor of 2 (*SI Material and Methods*).

We, therefore, set out to develop a live-cell fluorescence imaging workflow to measure fluorescence signal intensities of endogenously labeled Nups specifically at the NE. To implement it, we created a library of strains endogenously expressing C-terminally tagged Nups with yeast-optimized enhanced green fluorescent protein (yEGFP) preceded by a short flexible linker. To ensure that labeling does not interfere with Nup function and NPC incorporation, the logarithmic growth rates of all labeled stains were compared with wild-type cells (Fig. S1*A*) and the Nup-yEGFP localization together with the cellular morphology of the tagged strains were carefully examined. For the Nup Nic96, we also included an additional N-terminal GFP-tagged variant since the C-terminally tagged strain displayed a fitness defect manifesting in a delayed recovery from stationary phase (Fig. S3*A*). In total, we tagged and analyzed 26 different Nups.

To accurately quantify Nup-yEGFP intensities at the NE in an unbiased manner, we developed an automated image-processing pipeline (NuRIM). The NE was marked using the endoplasmic reticulum marker dsRed-HDEL. Yeast cells coexpressing various yEGFP-tagged Nups together with dsRed-HDEL were grown in parallel under the same conditions, and imaged side-by-side in an automated manner using identical microscope settings, both in bright field and for the dsRed and GFP channels (Fig. 1*A*). Bright-field images were used to avoid highly crowded areas (Fig. 1*A*, *i* and *ii*), while the dsRed channel was used to produce binary masks outlining the NE contours by an algorithm based on Laplacian edge detection (29) (Fig. 1*A*, *iii* and *iv*, and *SI Material and Methods*). These masks closely overlapped spatially with the Nup-yEGFP distribution, and their medial line (morphological skeleton) was used to compute corresponding background-corrected pixel intensities from the yEGFP channel (30) (Fig. 1*A*, *v* and *vi*). These values were averaged for each cell, image and yeast strain over thousands of nuclei to produce a final population average intensity value. *SI Material and Methods* provide a more systematic description of the rationale and the assumptions that underlie NuRIM.

An important assumption of our approach is that each individual Nup-yEGFP contributes linearly to the total intensity emitted from the NPC. To test this, we quantified the NPC intensities in a set of strains expressing individually labeled Nups, including Gle1, Nup42, Nup120, and Nup133, as well as the NPC-associated nuclear transport factor Mex67, and compared their intensities to the values obtained in double-labeled stains that coexpressed various pairs of these proteins. Within less than 5%, the fluorescence intensities of all tested double-labeled strains matched the values calculated by summing up the intensities of the two corresponding strains expressing a single Nup-yEGFP. This shows that our intensity measurements increase linearly in relation to copy number and can be used to measure relative abundance (Fig. 1*B*).

Another assumption is that neither crowding nor a different "microenvironment" in the NPC significantly influences fluorescence intensities and affects the accuracy of our measurements. Extreme proximity of EGFPs in oligomers can lead to quenching of fluorescence emission by homo-FRET (31, 32), and tight binding of anti-GFP antibodies to GFP was shown to modify fluorescence intensities (33). While the structural symmetries present in the NPC are expected to prevent such immediate contacts of individual GFP probes, we nevertheless set out to obtain evidence that the microenvironment does not significantly affect our intensity measurements. To this end, we introduced a 102-aa-long, flexible linker upstream of yEGFP in some of the strains. Such a long linker should release the yEGFP probes from their microenvironment—thus leading to a potential alteration of the fluorescence intensities. However, when we analyzed the corresponding signal intensities, no significant changes were observed compared with the results obtained with regular linkers (Fig. 1*C*).

Furthermore, for the correct interpretation of the NuRIM results, it is important that the spatial probability distribution (denoted p in *SI Material and Methods*) of the various analyzed Nups is identical. However, some Nups might be present in only a subset of NPCs or in additional, non-NPC pools at the NE. To recognize such unusual behavior, we compared the distribution patterns of all Nups in our library using normalized cumulative intensity distributions and the autocorrelation of intensities along the NE. For the majority of Nups, we observed highly similar signatures (Fig. S1 *B* and *C*). The three outliers, Ndc1, Mlp1, and Mlp2, are consistent with the additional presence of Ndc1 at the spindle pole body (34), and with the previously described absence of both Mlp1 and Mlp2 from NPCs in the nucleolar region (35) (Fig. S1*F*).

Although we were careful to perform all imaging experiments under very similar conditions, we also tested the robustness of NuRIM against inherent variability in culture density and the density of cells plated on the microscope slide (Fig. S1 *D* and *E*). To this end, we varied either of these parameters for one of the strains (Nup84-yEGFP) in the range ∼0.5× to 2× around the standard values used in the experiments and analyzed the impact on the NuRIM output. Within this range, we did not observe any significant influence on the readout (Fig. S1 *D* and *E*). Therefore, our imaging and quantification strategy is resilient against small unavoidable variations in cell culture and imaging conditions.

In summary, we conclude that NuRIM allows for an accurate and unbiased determination of the relative stoichiometry of endogenously labeled Nups within intact NPCs of living cells.

Determination of the Relative Nup Abundance. Next, we applied NuRIM to systematically quantify abundances for all Nups in our library (Fig. 1 *D* and *E*). To robustly compare sets of measurements performed on separate days, the average yEGFP intensity of six Y-complex components was used for normalization. The intensity readouts were highly reproducible and revealed a striking pattern of abundances (Fig. 1*E* and Table 1). The vast majority of Nups were present in very similar amounts, displaying values within 15% of each other (Fig. 1*E* and Table 1). This includes all members of the Y complex and the major components of the NPC scaffold. One exception was Nic96, which displayed an abundance of ∼1.5 for the C-terminally tagged version and an abundance of ∼2 for the N-terminal GFP variant (Fig. 1*E*, Table 1, and Fig. S3*B*). Since C-terminal tagging of

CELL BIOLOGY

Downloaded by guest on February 24, 2022

Table 1. Stoichiometry of Nups within the yeast NPC

NUPs	Fold ratio*	Absolute†	Eightfold‡
Nup85	1.11 ± 0.051	18.6	16
Nup120	1.01 ± 0.003	16.8	16
Nup84	0.83 ± 0.008	13.9 ± 2.8	16
Nup145C	1.03 ± 0.024	17.2	16
Nup133	1.01 ± 0.009	16.8	16
Seh1	1.03 ± 0.025	17.2	16
Nic96	1.39 ± 0.079	23.3	24
Nic96§	1.96 ± 0.016	32.8	32
Nup188	0.93 ± 0.034	15.6	16
Nup192	0.86 ± 0.008	14.3	16
Nup157	0.88 ± 0.005	14.7	16
Nup170	0.91 ± 0.009	15.2	16
Nup53	0.95 ± 0.014	15.9	16
Nup59	0.80 ± 0.048	13.3	16
Ndc1¶	1.18 ± 0.045	19.7	16
Pom34	0.97 ± 0.053	16.2	16
Pom152	0.43 ± 0.015	7.2	8
Nup1	0.77 ± 0.064	12.8	16
Nup60	0.90 ± 0.040	15.0	16
Nup116	0.88 ± 0.059	14.7	16
Nup100	0.89 ± 0.028	14.8	16
Nup159	0.89 ± 0.010	14.9	16
Nup42	0.38 ± 0.011	6.4	8
Nup82	0.91 ± 0.020	15.2	16
Gle1	0.42 ± 0.010	7.0	8
Mlp1¶	0.31 ± 0.004	5.2	
Mlp2¶	0.24 ± 0.005	3.9	

*Values obtained by normalizing to the Y complex except for Nic96§. Nic96§ represent values obtained for an N-terminally GFP-tagged Nic96 variant normalized to Nup120-GFP (Fig. S3). Mean ± SD. Values are obtained from three independent experiments.

†Absolute Nup copy numbers based on Nup84.

‡Eightfold rendered values were designated based on absolute Nup copy numbers.

§N-terminally GFP-tagged Nic96.

¶Nups that failed one of the controls (Fig. S1).

Nic96 led to a fitness defect, it is likely that Nic96 is twice as abundant as other scaffold Nups (Fig. 1*E*, Table 1, and Fig. S3*B*). By contrast, Pom152, Nup42, and Gle1 displayed distinctly lower values clustering around 0.5. The three outliers that are not evenly distributed along the NE, Ndc1, Mpl1, and Mlp2 are included for completeness (Table 1) but need to be viewed with prudence. Accordingly, the majority of Nups are present in the same copy number, and in general, Nups can be found in well-defined quanta, that is, ∼0.5, 1, or 2. Such distinct abundance classes are consistent with the eightfold symmetrical architecture of the NPC in which Nups are expected to be present in multiple copies of eight per structure.

Determination of Absolute Copy Numbers Reveals That Most Yeast Nups Are Present in 16 Copies per NPC. If the absolute NPC copy number was available for even a single Nup, our systematic ratiometric analysis would allow the determination of absolute copy numbers for all other Nups as well. We thus set out to quantify the total fluorescence intensity of a single NPC in cells expressing one of the fluorescently tagged Nups. Of note, endogenous tagging of Nups principally results in 100% labeling efficiency since all copies of the protein carry the fusion tag (but see also *Discussion*). We took advantage of the observation that single NPCs can occasionally be detected in dividing yeast cells where the part of the NE bridging the mother and daughter nuclei elongates and narrows (Movie S1) (36). These NPCs are more separated from their neighbors, allowing us to image and quantify the intensity of individual NPCs in several thousand cells using the Diatrack particle tracking software (37). As an absolute intensity reference, we also imaged in parallel, yeast-expressed rotavirus-like VP2 particles that contain exactly 120 copies of yEGFP (38). Furthermore, we recorded the intensity of single molecules of yEGFP adsorbed on glass coverslips (Movie S2). The intensity distributions of single yEGFP, Nup84-yEGFP NPCs, and VP2- yEGFP particles were fitted with a normal distribution. Comparison of their means showed that VP2 particles were 116 ± 7 times brighter than single yEGFP molecules, yielding an estimated copy number for Nup84-yEGFP of 13.9 ± 2.8 per NPC (Fig. 2*A*).

To validate this result, we performed an independent analysis using a different set of reference intensity markers: tetrahedral particles that contain precisely 12 or 24 GFP moieties (39). These particles contain "superfolder" GFP (sfGFP), a GFP variant with fast folding kinetics (40), and we therefore endogenously tagged several Nups including Gle1, Nup84, Nup120, and Nic96 also with sfGFP. As expected, tagging with sfGFP did not lead to any significant changes in the relative abundance readouts compared with yEGFP (Fig. S2*A*). Using the same methodology as before, we then recorded in parallel the absolute intensity distributions for 12× sfGFP and 24× sfGFP tetrahedral particles purified from *Escherichia coli*, and for the Nup84-sfGFP and Nup120-sfGFP NPCs in yeast. Based on the comparison of the means of the distributions, we determined absolute NPC copy numbers of 14.7 ± 2.5 for Nup84 and 15.8 ± 2.3 for Nup120 (Fig. 2*B* and Fig. S2*B*).

In accordance with these results, we assigned absolute stoichiometries for all Nups measured in Table 1. We conclude that the yeast NPC contains very close to 16 copies for most Nups (Table 1). These include major scaffold Nups constituting the framework of the NPC: the Y-complex members (Nup133, Nup120, Nup85, Nup84, Nup145C, Seh1) and the inner ring Nups (Nup188, Nup192, Nup157, Nup170). For Nic96, our relative abundance measurements led to an assignment of either 24 or 32 copies per NPC, depending on the position of the GFP tag (Fig. 1*E* and Table 1). This result was also confirmed by single NPC measurements where Nic96-yEGFP was 1.37 ± 0.1 times brighter than Nup120-yEGFP, and the N-terminal GFP-Nic96 variant displayed a 1.93 ± 0.14 higher brightness compared with Nup120-GFP (Fig. S3 *C* and *D*). Overall, the copy numbers obtained here for budding yeast are in stark contrast to the human NPC where corresponding proteins were reported to be generally twice as abundant, including 32 copies of the Y complex (16, 21–23).

The astonishing differences in NPC composition between yeast and human prompted us to develop another independent method to examine NPC stoichiometry. The characteristic intensity spots (i.e., speckles) that are observed by fluorescence microscopy in the yeast interphase NE are produced by randomly overlapping, diffraction-limited images of several closely positioned NPCs (Fig. 2*C*, *iv*). Precise determination of a characteristic "NPC clustering" factor within such spots would allow us to estimate an absolute stoichiometry by comparing their intensities with established external fluorescence standards. We thus developed a 3D mathematical model of the NE based on NPC density data derived from 3D EM reconstructions (36) and on classical image formation theory (*SI Material and Methods*). This model allowed us to estimate the characteristic NPC clustering factor predicting that on average 3.7 NPCs are present in such NPC intensity spots (*SI Material and Methods*). Three-dimensional stacks acquired for Nup84-yEGFP– and VP2-yEGFP–expressing cells imaged under identical conditions were then used as inputs to quantify absolute signal intensities. By comparing the intensity distributions of the NPCs spots and the VP2 particles, we computed a copy number of 13.8 ± 4 for Nup84 per NPC. This result is fully consistent with and confirms our measurements based on single NPC intensities (Fig. 2*C*).

Altogether, our results demonstrate that on average no more than 16 copies of Nup84 are present in the yeast NPC. Based on

Downloaded by guest on February 24, 2022

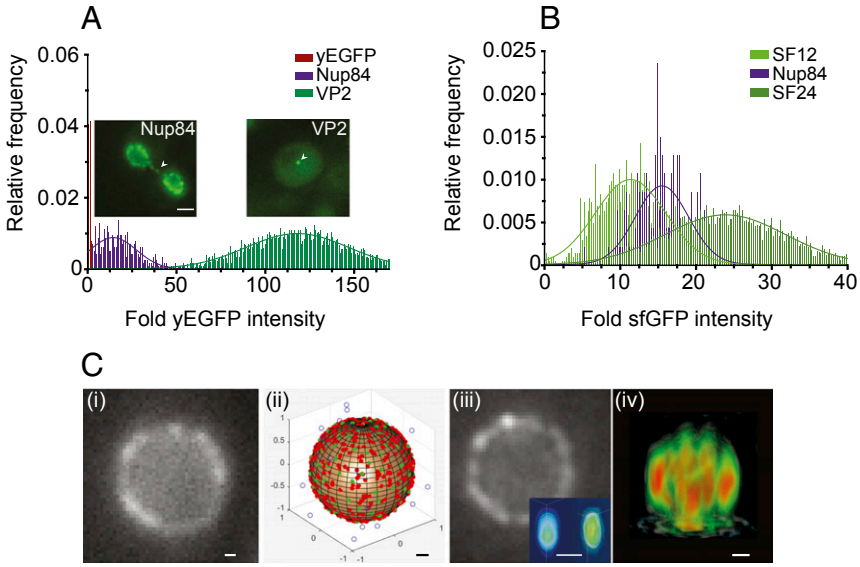

Fig. 2. Absolute stoichiometry of yeast Nups. (*A*) Representative intensity histograms and Gaussian fits (smooth lines) obtained for single yEGFP molecules, single NPCs in regions between separating nuclei in Nup84-yEGFP–expressing yeast cells (arrowhead), and for the yeast-expressed 120-mer VP2-yEGFP particles (arrowhead). (Scale bars: 2 μm.) (*B*) Intensity histograms and fits are displayed similar to *A* for single NPCs in Nup84-sfGFP–expressing yeast cells, and for purified SF12 and SF24 particles containing 12 and 24 sfGFP molecules, respectively. (*C, i*) Representative fluorescence microscopy image showing localization of Nup84-yEGFP–labeled NPCs. (*C, ii*) Computational model of the NE. NPCs are represented as green dots, dsRed-HDEL as red dots, and dim sources simulating background fluorescence as blue dots. (*C, iii*) Simulated image of the NE produced computationally from the model *ii*. Note good resemblance to genuine Nup84-yEGFP localization (compare with *i*). *Inset* compares computed PSF with experimentally acquired PSF. (*C, iv*) Representative 3D rendering of image stack shows heat map of intensities in Nup84-yEGFP cells illustrating high-intensity spots or "speckles" (red) produced due to stochastic overlap of the ∼120 NPCs. (Scale bar: 200 nm.)

our relative abundance measurements, most Nups within the NPC of budding yeast, therefore, exist in 16 copies. This finding is consistent with molecular mass estimates for the yeast NPC, which is significantly smaller compared with its vertebrate counterpart (24, 25). Furthermore, this suggests that there are considerable differences in the architectural organization of the yeast and vertebrate NPCs. From an evolutionary perspective, this implies that a macromolecular machine with conserved function and constructed from conserved subunits can adopt fundamentally distinct structural layouts in different species.

Altering Nup Expression Leads to NPCs with Different Stoichiometries. Our automated imaging pipeline can also be applied to mutant yeast strains in which the composition of the NPC is altered. This paves the way for investigating a wide range of questions regarding the NPC architecture that would have otherwise been difficult to address. For example, in recently proposed models of the human NPC (22, 23), Nup155 is an abundant Nup present in 48 copies playing a critical role in linking the Y complex to the NPC core inner ring and nuclear membrane. However, despite this central structural role, in yeast, its function is split between two nonessential and functionally redundant paralogous genes *NUP170* and *NUP157* that have separated due to whole-genome duplication ∼100 Mya (41–43). Of note, each of these Nups is present in only ∼16 copies in the yeast NPC (Table 1). To study this further, we utilized NuRIM to investigate whether Nup157 can replace Nup170 when the *NUP170* gene is deleted. We hypothesized that if substitution was to occur, we should see an increase in the intensity due to additional copies of Nup157 now at the pore. However, in *NUP157-yEGFP* cells, the deletion of *NUP170* did not cause any increase in Nup157-yEGFP intensity (Fig. 3 *A* and *B*), indicating that sites that are normally occupied by Nup170 remain empty in its absence. To rule out the possibility that protein expression is a limiting factor for substitution, we constructed a *NUP157-yEGFP nup170Δ* strain that contained an extra copy of *NUP157-yEGFP* inserted into the *URA3* locus, thus doubling the production of this protein. This, however, also did not cause any significant increase in its abundance at the NPC. In contrast and as expected, the reexpression of *NUP170* by insertion of a *NUP170-yEGFP* gene into the URA3 locus produced twice as bright NPCs (Fig. 3 *A* and *B*). We conclude that Nup157-yEGFP is not able to substitute for the loss of Nup170, indicating that yeast NPCs with only ∼16 copies of Nup157 are fully functional.

Gene duplications supply the raw material for the emergence of new functions through the forces of mutation and natural selection (44). We therefore also wanted to test the inverse scenario, that is, whether Nup170 could substitute for the loss of Nup157 at the NPC. As in the mirror strain, we did not observe any increase in abundance of Nup170-yEGFP upon deletion of *NUP157* (Fig. 3 *C* and *D*). However, in this case, the introduction of an additional copy of *NUP170-yEGFP* led to a twofold increase in Nup170 abundance at the NPC as measured by NuRIM (Fig. 3 *C* and *D*). This intensity increase was further confirmed by brightness measurements of individual NPCs, and *nup157Δ* cells expressing two copies of Nup170-yEGFP exhibited a 2.07 ± 0.26-fold higher NPC intensity compared with cells expressing a single Nup170-yEGFP copy (Fig. 3*G*). This reveals an interesting functional asymmetry between these two paralogs and shows that gene expression levels can affect the NPC stoichiometry producing an NPC with ∼32 copies of Nup170.

Motivated by these findings, we also investigated another paralog pair, comprised of Nup188 and Nup192. These two paralogs presumably originated from an ancient gene duplication event—about 800 Mya (45). Since the gene encoding for Nup192 is essential, we restricted our analysis to the deletion of *NUP188*. Similar to the results with Nup170 and Nup157, no intensity increase was observed in *nup188Δ* cells in the presence of endogeneous levels of Nup192-yEGFP (Fig. 3 *E* and *F*). However, once an extra copy of *NUP192-yEGFP* was introduced, an increase in NPC abundance of more than 50% was detected (Fig. 3 *E* and *F*). This suggests that Nup192 is capable of occupying the empty Nup188 sites, but it is unable to do so entirely. Taken together,

Downloaded by guest on February 24, 2022

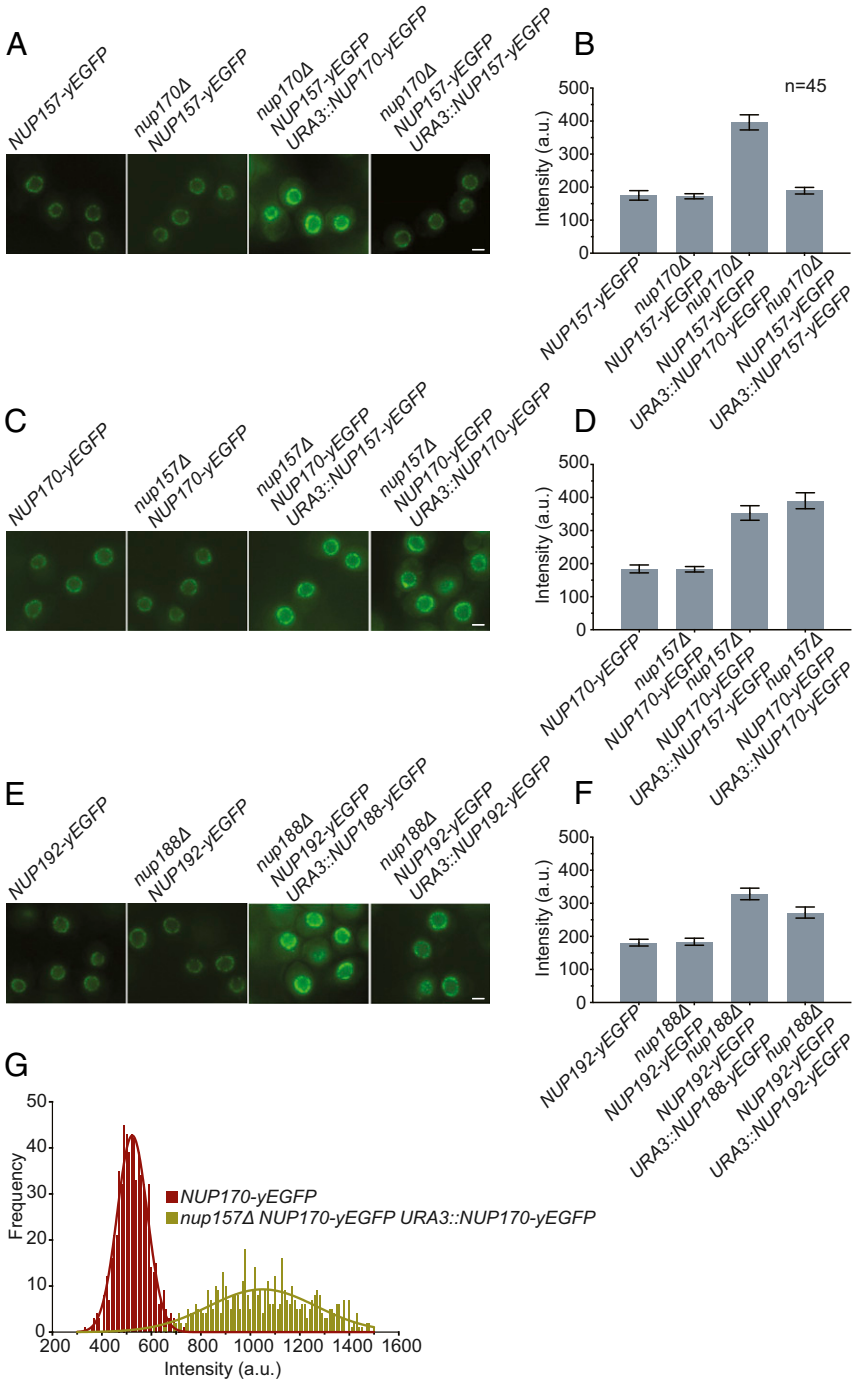

Fig. 3. Analysis of Nup stoichiometry in yeast mutants. (*A*, *C*, and *E*) Representative images illustrating Nup-yEGFP localization in actively growing yeast cells with specified genotypes. The corresponding NE intensities quantified using NuRIM are shown in *B*, *D*, and *F*, respectively. Mean ± SD. *n*, number of image frames analyzed for *B*, *D*, and *F*. (Scale bars: 2 μm.) (*G*) Representative intensity histograms and Gaussian fits obtained for single NPCs in *NUP170-yEGFP* and *NUP170-yEGFP nup170Δ URA3::NUP170-yEGFP* strains.

these results identify intriguing redundancies between Nup paralogs and reveal a remarkable compositional plasticity of the NPC.

Discussion and Conclusion

The inventory of Nups that make up the NPC has been biochemically characterized in several organisms from diverse branches of the eukaryotic evolutionary tree (2–5). Whereas individual components of this inventory are largely well conserved, it has been unclear to which extent this is also true for the architecture of the entire NPC. To understand how the vast number of NPC building blocks come together to produce a functional structure requires various sources of high-quality data including precise information about the copy number for each Nup subunit (28). In this study, we have developed a strategy based on live-cell imaging to accurately determine the absolute stoichiometry for the majority of Nups within the intact budding

Downloaded by guest on February 24, 2022

yeast NPC and applied this approach to begin to probe the principles underlying the structural organization of the NPC using Nup mutants. Our analyses revealed striking differences between yeast and human NPCs and exposed an inherent compositional plasticity of the NPC architecture.

In budding yeast, NPCs are densely packed within the NE (36), preventing resolution of individual structures by light microscopy. However, NPCs containing twice as many copies of GFP-labeled Nup when imaged identically will nevertheless give rise to NEs that are twice as bright. Our approach to determine the stoichiometry of the NPC was based on this principle and relied on precise measurement of fluorescence intensities of endogenously GFP-tagged Nups at the NE to evaluate their relative abundance (46) (Fig. 1*E*). These measurements were automated and subjected to multiple layers of quality control to ensure that the results (*i*) are linearly dependent on the Nup copy number, (*ii*) are highly reproducible between multiple measurements of thousands of nuclei, (*iii*) are robust to small variations in experimental conditions, and (*iv*) are not influenced by variations in the GFP microenvironment for the various tagged Nups (Fig. 1 and Fig. S1). The relative stoichiometries obtained with this approach are consistent with an eightfold symmetrical NPC organization, showing that all 23 Nups that could be reliably measured cluster around distinct quanta of abundance. In our analysis, we found that three Nups, Ndc1, Mlp1, and Mlp2, displayed an atypical distribution pattern in the NE, and also these three outliers deviated from the discrete abundance pattern of other Nups (Fig. 1*E* and Table 1). The numerical value for the abundance of Ndc1, which is slightly higher compared with the Y-complex members, is likely explained by the additional presence of Ndc1 at the spindle pole body (34), whereas the exceptionally low values for Mlp1 and Mlp2 is consistent with their absence from a subset of NPCs (Fig. 1*E*, Table 1, and Fig. S1*F*).

Overall, compared with a previous comprehensive stoichiometry analysis in yeast by Rout et al. (4), our results are in good agreement for symmetric core Nups showing approximately similar relative abundances but differ significantly for several peripheral Nups, which we find in higher amounts (Fig. 1*E* and Table 1). This discrepancy could be explained by a partial loss of peripheral Nups that might be difficult to avoid during the biochemical purification of the NEs used in this prior work. Interestingly, distinct copy numbers of yeast Nups were previously also reported using step bleaching of single NPCs with an intense laser spot at the NE (17). However, since the punctae seen with fluorescently labeled NPCs in regular regions of yeast interphase NE mostly do not correspond to single structures but to the randomly overlapping images of at least a few of them, it is unclear to us how imaging of single NPCs was guaranteed in this study (Fig. 2*C*) or how NPCs were immobilized over the timescale of several seconds needed for recording photobleaching curves.

In mammalian cells, the typical distance between neighboring NPCs in the NE generally lies above the Abbe resolution limit (10), making it possible to characterize fluorescence signals from NPCs one at a time with optical microscopy (47). As pointed out, this is not the case in interphase budding yeast cells, but during cell division the NE between the dividing mother and daughter nuclei extends and narrows, which distributes individual NPCs in this region sufficiently to resolve them by light microscopy (36). We used this phenomenon to quantify absolute Nup copy numbers within individual NPCs by precise brightness measurements of GFP-tagged yeast strains and comparing those to a set of fluorescence standards with a defined number of identical GFP molecules. The copy number values that we determined for two different Y-complex members, Nup84 and Nup120, were close to 16 copies per NPC. Very similar copy numbers were obtained with different fluorescent tags and fluorescent standards (Fig. 2 and Fig. S2). Moreover, the conclusion that there are 16 copies of Nup84 per NPC was further confirmed by a 3D modeling approach that was based on the measured NPC density (36) and absolute intensity measurements of NPC clusters in interphase NEs (Fig. 2*C*). Potentially, our estimation of absolute copy numbers could be influenced by GFP maturation time, resulting in different fractions of fluorescent GFP molecules in NPCs or in our standards. While this could explain why we find copy numbers for Y-complex components that are slightly below 16, the contribution of GFP maturation time is not a significant source of error since similar values were obtained using both yEGFP and sfGFP, which have different maturation kinetics (48).

Based on intensity measurements with both NuRIM and at the single NPC level, we detect either 24 or 32 copies of Nic96 per NPC depending on whether the GFP tag is placed at the C or N terminus of Nic96 (Table 1 and Fig. S3 *C* and *D*). Considering that C-terminal tagging of Nic96 caused a detectable fitness defect, and these cells displayed a delay in exiting stationary phase compared with cells expressing wild type or the N-terminally tagged variant (Fig. S3*A*), it is likely that the presence of GFP on the C terminus of Nic96 prevents its complete incorporation into the NPC. A copy number of 32 for Nic96 would also be consistent with the evolutionarily conserved ability of Nic96 to form binary complexes with Nup188 and Nup192 that we found to be present in 16 copies each in yeast (49, 50). Irrespectively, our results show that functional NPCs can be built with either 24 or 32 copies of Nic96, underscoring the inherent plasticity of the NPC architecture.

Based on our relative abundance and absolute copy number measurements, the vast majority of yeast Nups are present in no more than 16 copies per NPC (Fig. 1*E* and Table 1). This fits well with prior total mass estimates of 45–70 MDa for the yeast NPC (24, 25), but reveals a remarkable difference in the structural organization compared with the mammalian NPC: many yeast structural core Nups are present in ∼50% lower amounts per NPC compared with their mammalian counterparts (18). One particularly prominent difference is the copy number of the Y complex (also Nup107 or Nup84 complex), an evolutionarily conserved architectural element of the NPC accounting for approximately one-third of its total mass, for which we find 16 copies in yeast whereas 32 copies were assigned for the mammalian NPC. Since structural analyses of the mammalian NPC show a peculiar arrangement of the Y complex in two concentric rings on each side of the NPC (16, 21–23), it is likely that the yeast NPC contains only one such ring on the nuclear and cytoplasmic side, respectively. Another obvious difference concerns the vertebrate Nup155 (Nup170 and Nup157 in yeast), which forms multiple important connections, including links to the Y complex, to other core Nups, and to the nuclear membrane (51). It is present in 48 copies in the mammalian NPC (22, 23), whereas yeast contains only 16 copies for each of its two paralogs, Nup170 and Nup157, amounting to a total maximum of 32 copies (Fig. 1*E* and Table 1). Similarly, the evolutionarily conserved paralog pair Nup188 and Nup205 (Nup188 and Nup192 in yeast) is present in 16 and 32 copies in mammalian NPC (23), while the yeast NPC contains only 16 copies of each (Fig. 1*E* and Table 1), suggesting that these conserved paralogs also differ in their abundances between the two species.

These intriguing differences raise the question of how the same set of conserved Nups can produce assemblies that are so diverse in their architectural layout and yet remain functionally equivalent. To begin addressing this, we employed our quantitative approach to analyze the stoichiometry of NPCs in cells that had altered expression of several Nups. First, this showcased that the NPC scaffold is remarkably robust and has multiple inbuilt redundancies. For example, the presence of one-half the copy number of the Nup170/157 paralog pair is sufficient for viability, indicating that NPCs that are built in the absence of either member contain voids in their structure, yet remain fully

Downloaded by guest on February 24, 2022

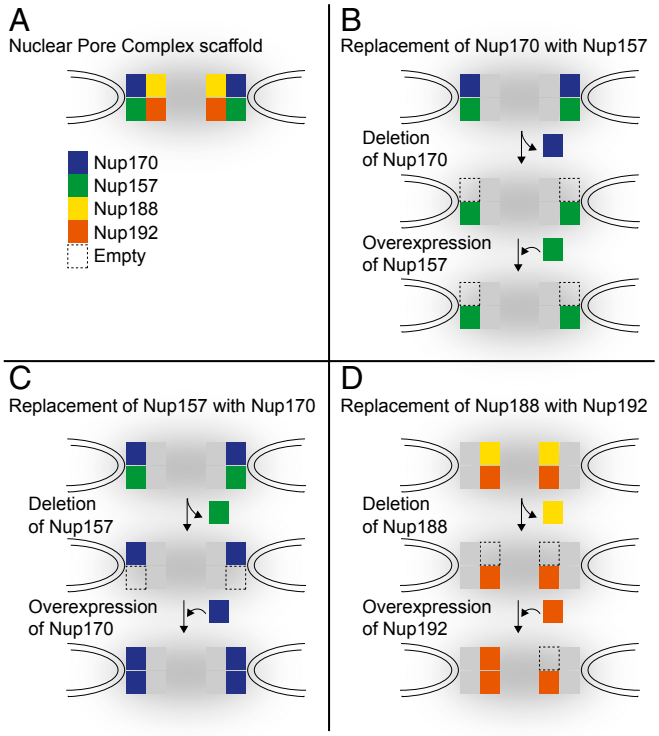

Fig. 4. Modular organization of the NPC. (*A*) Schematic of the NPC scaffold. (*B–D*) Illustration depicting the experimental outcomes shown in Fig. 3.

functional (Figs. 3 *A–D* and 4 *B* and *C*). Second, our analyses revealed an astonishing compositional flexibility of the NPC architecture. Overexpression of one of the paralogs, Nup170, in the absence of Nup157 produced NPCs that contained 32 copies of solely Nup170 (Figs. 3 *C*, *D*, and *G* and 4*C*). By contrast, Nup157 was unable to substitute for Nup170 even when overexpressed (Figs. 3 *A* and *B* and 4*A*). These differences might be due to the more limited NPC interactions of Nup157 compared with Nup170, since it was previously shown that Nup170 can bind to both membrane-associated Nups Nup53 and Nup59, whereas Nup157 is only able to interact with Nup53 (52). Even more surprisingly, similar changes in NPC stoichiometry were observed for the Nup192/Nup188 paralog pair (Figs. 3 *E* and *F* and 4*D*). These paralogs separated very early during eukaryotic evolution and share only low sequence similarity; however, our observations are compatible with the structural and functional similarities that can be found among homologs of these Nups from various species (45, 49).

Altogether, our results reveal that the composition of the NPC has inherent plasticity and, for example, can be altered by varying the expression levels of its subunits. This could explain how variations, initially driven by alterations in expression levels could result in stable changes in the overall layout of the NPC structure over the course of evolution. Other sources of change may include the acquisition of new NPC components. For instance, the outer Y-complex ring accounting for ∼25% difference in the copy number between the human and yeast NPC, is attached to the human NPC via Nup358, a Nup that is not present at all in yeast (21). This compositional plasticity suggests that the organization of the NPC is modular, following a "Lego-like" principle, where a set of common components can be utilized to form distinct structures with increasing complexity (Fig. 4). In support of this view, several highly structured NPC subunits are chiefly connected by highly flexible, disordered motifs, such as short linear motifs or FG repeats to ensure NPC stability (51, 53). This modularity could also be a reflection of the shared ancestry of core components of the NPC and COP-coats, in which changes in coatomer copy number drive structural diversity (54, 55). Moreover, our results raise a possibility that NPCs even within a single cell could display variability in composition or architecture. Intriguingly, observations made in the binucleate ciliate, *Tetrahymena thermophile*, showed that paralogs of Nup214 and Nup153 can localize specifically to either micronuclear or macronuclear NPCs within the same cell (56).

In conclusion, we have developed a robust method to accurately quantify both relative and absolute copy numbers for Nups within the yeast NPC. The results of our Nup stoichiometry measurements provide an important resource for the generation of high-resolution models of the NPC. Furthermore, our approach can be easily implemented and applied to other cell-biological questions; for example, it may be used to study NPC biogenesis, to analyze NPCs from other species, or even to examine other multisubunit complexes in the NE.

Materials and Methods

Yeast Strains and Plasmids. The growth media, *Saccharomyces cerevisiae* strains, and plasmids used in this study were produced using standard yeast and molecular cloning protocols, and are listed in Tables S1 and S2.

Growth Tests. Yeast strains were grown in synthetic complete medium containing 2% dextrose (SCD). OD_{600} measurements were acquired over 24 h using CLARIOstar automated plate reader (BMG Labtech) at 30 °C in 24-well plates (Nunc) from overnight precultures diluted 1:125 in SCD. Log-phase duplication times (Fig. S1*A*) were determined from the OD_{600} reads as average duplication time t_{dup} over the duration of log phase, a period when t_{dup} reaches minimum and stays approximately constant. t_{dup} was calculated as $\Delta t/\mathrm{Log2}(OD_{t+\Delta t}/OD_t)$, where $OD_{t+\Delta t}$ and OD_t are OD_{600} values at consequent reads and Δt time between the reads.

Purification of Tetrahedral Particles. The tetrahedral particles (both SF12 and SF24) were expressed and purified from *E*. coli (BL21 DE3) as previously described in ref. 57.

Fluorescence Microscopy Techniques. Yeast cells endogenously expressing yEGFP-tagged Nups were grown to log phase and imaged in ConA-coated glass bottom plates (MatriPlate) using an inverted epifluorescence Ti microscope (Nikon) equipped with a Spectra X LED light source (Lumencore) and Flash 4.0 scMOS camera (Hamamatsu) with the 100× Plan-Apo VC objective, N.A. 1.4 (Nikon). The NIS Elements software (Nikon) was used for image acquisition. All yeast strains used for the quantitative analysis of Nup-yEGFP intensity also expressed dsRed-HDEL. Image segmentation and GFP signal quantification were performed as outlined in *SI Material and Methods*.

Imaging of the tetrahedral particles was done by mounting them on agarose pads for microscopy as previously described in ref. 58.

Image quantification and modeling were conducted as described in *SI Material and Methods*.

ACKNOWLEDGMENTS. We are grateful to E. Dultz, A. Kralt, and other K.W. laboratory members for helpful discussions and suggestions and also to B. Hofland for preparation of various experimental materials. We are indebted to D. Baker (University of Washington) for providing the tetrahedral constructs, and we thank J. Cohent (Institut National de la Recherche Agronomique) for the VP2 construct, S. Wente (Vanderbilt University) for the GFP-Nic96 construct, and C. Weber for preparing a VP2-expressing yeast strain. This work was supported by Swiss National Science Foundation Grant SNF 159731 (to K.W.).

1. Watson ML (1954) Pores in the mammalian nuclear membrane. *Biochim Biophys Acta* 15:475–479.
2. Cronshaw JM, Krutchinsky AN, Zhang W, Chait BT, Matunis MJ (2002) Proteomic analysis of the mammalian nuclear pore complex. *J Cell Biol* 158:915–927.
3. DeGrasse JA, et al. (2009) Evidence for a shared nuclear pore complex architecture that is conserved from the last common eukaryotic ancestor. *Mol Cell Proteomics* 8:2119–2130.
4. Rout MP, et al. (2000) The yeast nuclear pore complex: Composition, architecture, and transport mechanism. *J Cell Biol* 148:635–651.

Downloaded by guest on February 24, 2022

5. Tamura K, Fukao Y, Iwamoto M, Haraguchi T, Hara-Nishimura I (2010) Identification and characterization of nuclear pore complex components in *Arabidopsis thaliana*. *Plant Cell* 22:4084–4097.
6. Gall JG (1967) Octagonal nuclear pores. *J Cell Biol* 32:391–399.
7. Alber F, et al. (2007) The molecular architecture of the nuclear pore complex. *Nature* 450:695–701.
8. Ori A, Singer S, Beck M (2014) Protein complex composition distinguishes different cancer types. *Eur J Cancer* 50(Suppl 5):S131.
9. Sakiyama Y, Mazur A, Kapinos LE, Lim RYH (2016) Spatiotemporal dynamics of the nuclear pore complex transport barrier resolved by high-speed atomic force microscopy. *Nat Nanotechnol* 11:719–723.
10. Szymborska A, et al. (2013) Nuclear pore scaffold structure analyzed by super-resolution microscopy and particle averaging. *Science* 341:655–658.
11. Hoelz A, Glavy JS, Beck M (2016) Toward the atomic structure of the nuclear pore complex: When top down meets bottom up. *Nat Struct Mol Biol* 23:624–630.
12. Knockenhauer KE, Schwartz TU (2016) The nuclear pore complex as a flexible and dynamic gate. *Cell* 164:1162–1171.
13. Kampmann M, Blobel G (2009) Three-dimensional structure and flexibility of a membrane-coating module of the nuclear pore complex. *Nat Struct Mol Biol* 16: 782–788.
14. Kelley K, Knockenhauer KE, Kabachinski G, Schwartz TU (2015) Atomic structure of the Y complex of the nuclear pore. *Nat Struct Mol Biol* 22:425–431.
15. Stuwe T, et al. (2015) Nuclear pores. Architecture of the nuclear pore complex coat. *Science* 347:1148–1152.
16. Bui KH, et al. (2013) Integrated structural analysis of the human nuclear pore complex scaffold. *Cell* 155:1233–1243.
17. Mi L, Goryaynov A, Lindquist A, Rexach M, Yang W (2015) Quantifying nucleoporin stoichiometry inside single nuclear pore complexes in vivo. *Sci Rep* 5:9372.
18. Ori A, et al. (2013) Cell type-specific nuclear pores: A case in point for context-dependent stoichiometry of molecular machines. *Mol Syst Biol* 9:648.
19. Tie HC, Madugula V, Lu L (2016) The development of a single molecule fluorescence standard and its application in estimating the stoichiometry of the nuclear pore complex. *Biochem Biophys Res Commun* 478:1694–1699.
20. Eibauer M, et al. (2015) Structure and gating of the nuclear pore complex. *Nat Commun* 6:7532.
21. von Appen A, et al. (2015) In situ structural analysis of the human nuclear pore complex. *Nature* 526:140–143.
22. Kosinski J, et al. (2016) Molecular architecture of the inner ring scaffold of the human nuclear pore complex. *Science* 352:363–365.
23. Lin DH, et al. (2016) Architecture of the symmetric core of the nuclear pore. *Science* 352:aaf1015.
24. Rout MP, Blobel G (1993) Isolation of the yeast nuclear pore complex. *J Cell Biol* 123: 771–783.
25. Yang Q, Rout MP, Akey CW (1998) Three-dimensional architecture of the isolated yeast nuclear pore complex: Functional and evolutionary implications. *Mol Cell* 1: 223–234.
26. Grossman E, Medalia O, Zwerger M (2012) Functional architecture of the nuclear pore complex. *Annu Rev Biophys* 41:557–584.
27. Reichelt R, et al. (1990) Correlation between structure and mass distribution of the nuclear pore complex and of distinct pore complex components. *J Cell Biol* 110: 883–894.
28. Lasker K, Sali A, Wolfson HJ (2010) Determining macromolecular assembly structures by molecular docking and fitting into an electron density map. *Proteins* 78: 3205–3211.
29. Vallotton P, et al. (2009) Segmentation and tracking individual Pseudomonas aeruginosa bacteria in dense populations of motile cells. *2009 24th International Conference Image and Vision Computing New Zealand (IVCNZ 2009)* (IEEE Press, New York), pp 221–225.
30. Soille P (2003) *Morphological Image Analysis Principles and Applications* (Springer, Berlin), 2nd Ed.
31. Kruitwagen T, Denoth-Lippuner A, Wilkins BJ, Neumann H, Barral Y (2015) Axial contraction and short-range compaction of chromatin synergistically promote mitotic chromosome condensation. *eLife* 4:e1039.
32. Vámosi G, et al. (2016) EGFP oligomers as natural fluorescence and hydrodynamic standards. *Sci Rep* 6:33022.
33. Pavoor TV, Cho YK, Shusta EV (2009) Development of GFP-based biosensors possessing the binding properties of antibodies. *Proc Natl Acad Sci USA* 106: 11895–11900.
34. Chial HJ, Rout MP, Giddings TH, Winey M (1998) Saccharomyces cerevisiae Ndc1p is a shared component of nuclear pore complexes and spindle pole bodies. *J Cell Biol* 143: 1789–1800.
35. Galy V, et al. (2004) Nuclear retention of unspliced mRNAs in yeast is mediated by perinuclear Mlp1. *Cell* 116:63–73.
36. Winey M, Yarar D, Giddings TH, Jr, Mastronarde DN (1997) Nuclear pore complex number and distribution throughout the Saccharomyces cerevisiae cell cycle by three-dimensional reconstruction from electron micrographs of nuclear envelopes. *Mol Biol Cell* 8:2119–2132.
37. Vallotton P, et al. (2017) Diatrack particle tracking software: Review of applications and performance evaluation. *Traffic* 18:840–852.
38. Charpilienne A, et al. (2001) Individual rotavirus-like particles containing 120 molecules of fluorescent protein are visible in living cells. *J Biol Chem* 276:29361–29367.
39. King NP, et al. (2014) Accurate design of co-assembling multi-component protein nanomaterials. *Nature* 510:103–108.
40. Pedelacq JD, Cabantous S, Tran T, Terwilliger TC, Waldo GS (2006) Engineering and characterization of a superfolder green fluorescent protein. *Nat Biotechnol* 24:79–88.
41. Kellis M, Birren BW, Lander ES (2004) Proof and evolutionary analysis of ancient genome duplication in the yeast *Saccharomyces cerevisiae*. *Nature* 428:617–624.
42. Koszul R, Caburet S, Dujon B, Fischer G (2004) Eucaryotic genome evolution through the spontaneous duplication of large chromosomal segments. *EMBO J* 23:234–243.
43. Marelli M, Aitchison JD, Wozniak RW (1998) Specific binding of the karyopherin Kap121p to a subunit of the nuclear pore complex containing Nup53p, Nup59p, and Nup170p. *J Cell Biol* 143:1813–1830.
44. Ohno S, Wolf U, Atkin NB (1968) Evolution from fish to mammals by gene duplication. *Hereditas* 59:169–187.
45. Andersen KR, et al. (2013) Scaffold nucleoporins Nup188 and Nup192 share structural and functional properties with nuclear transport receptors. *eLife* 2:e00745.
46. Vallotton P, et al. (2012) Automating the quantification of membrane proteins under confocal microscopy. *2012 9th IEEE International Symposium on Biomedical Imaging (ISBI)* (IEEE Press, New York), pp 776–779.
47. Rabut G, Doye V, Ellenberg J (2004) Mapping the dynamic organization of the nuclear pore complex inside single living cells. *Nat Cell Biol* 6:1114–1121.
48. Pédelacq JD, Cabantous S, Tran T, Terwilliger TC, Waldo GS (2006) Engineering and characterization of a superfolder green fluorescent protein. *Nat Biotechnol* 24:79–88.
49. Amlacher S, et al. (2011) Insight into structure and assembly of the nuclear pore complex by utilizing the genome of a eukaryotic thermophile. *Cell* 146:277–289.
50. Flemming D, et al. (2012) Analysis of the yeast nucleoporin Nup188 reveals a conserved S-like structure with similarity to karyopherins. *J Struct Biol* 177:99–105.
51. Beck M, Hurt E (2017) The nuclear pore complex: Understanding its function through structural insight. *Nat Rev Mol Cell Biol* 18:73–89.
52. Onischenko E, Stanton LH, Madrid AS, Kieselbach T, Weis K (2009) Role of the Ndc1 interaction network in yeast nuclear pore complex assembly and maintenance. *J Cell Biol* 185:475–491.
53. Onischenko E, et al. (2017) Natively unfolded FG repeats stabilize the structure of the nuclear pore complex. *Cell* 171:904–917.e19.
54. Devos D, et al. (2005) Components of coated vesicles and nuclear pore complexes share a common molecular architecture. *PLoS Biol* 3:350, and erratum (2005) 3:e80.
55. Onischenko E, Weis K (2011) Nuclear pore complex—a coat specifically tailored for the nuclear envelope. *Curr Opin Cell Biol* 23:293–301.
56. Iwamoto M, et al. (2017) Compositionally distinct nuclear pore complexes of functionally distinct dimorphic nuclei in the ciliate *Tetrahymena*. *J Cell Sci* 130:1822–1834.
57. Hsia Y, et al. (2016) Corrigendum: Design of a hyperstable 60-subunit protein icosahedron. *Nature* 540:150.
58. Shimogawa MM, Wargacki MM, Muller EG, Davis TN (2010) Laterally attached kinetochores recruit the checkpoint protein Bub1, but satisfy the spindle checkpoint. *Cell Cycle* 9:3619–3628.

Downloaded by guest on February 24, 2022